The Role of Thermalization in the Cooling Dynamics of Hot Carrier Solar Cells

Faber, Tim; Filipovic, Lado; Koster, L. Jan Anton

[Link to publication in University of Groningen/UMCG research database](#)

The Role of Thermalization in the Cooling Dynamics of Hot Carrier Solar Cells

*Tim Faber, Lado Filipovic, and L. Jan Anton Koster**

The hot carrier solar cell (HCSC) concept has been proposed to overcome the Shockley Queisser limit of a single p–n junction solar cell by harvesting carriers before they have lost their surplus energy. A promising family of materials for these purposes is metal halide perovskites (MHP). MHPs have experimentally shown very long cooling times, the key requirement of a HCSC. By using ensemble Monte Carlo simulations, light is shed on why cooling times are found to be extended. This article concentrates on the role of thermalization in the cooling process. The role of carrier–phonon and carrier–carrier interactions in thermalization and cooling is specified, while showing how these processes depend on material parameters, such as the dielectric constant and effective mass. It is quantified how thermalization acts as a cooling mechanism via the cold background effect. The importance of a low degree of background doping is to achieve the observed extended cooling times. Herein, it is mapped out how perovskites should be tuned, their material parameters, carrier concentration, and purity, in order to realize a HCSC. It contributes to the debate on the cooling times in MHPs and the suitability of tin perovskites for HCSCs.

1. Introduction

Hot carrier solar cells (HCSC) have been proposed as a means to overcome the Shockley Queisser (SQ) limit,[1] the theoretical efficiency limit for a single junction solar cell.[2,3] The rationale behind the SQ limit is threefold: One photon can only create a single electron-hole pair, the solar cell is under unconcentrated illumination, and all excess energy is transferred to the lattice via thermal relaxation. By harvesting charge carriers before they

have lost their surplus energy in the form of heat, the theoretical power conversion efficiency (PCE) could be boosted up to 66% under 1 sun illumination.[4] However, as carriers typically cool down within 100 fs,[5] the realization of a HCSC has appeared to be a daunting task and, until the present day, no working device has been presented.

More recently, a resurgence of interest in HCSC designs has been initiated by reports of metal halide perovskites (MHP) showing unusually long cooling times (see **Table 1**).[6] MHPs have already been in the center of the attention for quite some time for their excellent opto-electronic properties, while being solution processable and cost efficient.[7] Intriguingly, the experimental reports on slow cooling in MHPs show significant variation in their results, triggering a scientific debate on the physical explanations behind this phenomenon.[8–12] As slow cooling is essential for the realization of working HCSCs, the discussion calls for a deeper theoretical understanding and further research on this topic.

The proposed design of HCSCs is depicted in **Figure 1**, and it depends on several factors.[13] The most important is an absorber layer which presents extended relaxation times, i.e., carriers must lose their energy as slowly as possible, since only then does it become possible to extract them while they are still hot. Obviously, the absorber layer must also possess features of "normal" PV materials, such as a reasonably high mobility and broad spectral absorption.[1]

A second critical aspect of HCSCs is that carriers are extracted to the contacts with the help of energy selective contacts (ESC).[13,14] The energy levels of these contacts are aligned with the hot carrier distributions at temperatures T_e and T_h (see Figure 1), enabling the extraction of carriers while they are still hot. ESCs are small bandwidth (≈ 0.1 eV), large bandgap materials, which transport carriers *isentropically* to the contacts, maintaining the large energy difference (ΔE_{eh}) between the quasi–Fermi levels and hence resulting in an enhanced open circuit voltage.[14]

After photo-excitation (Step 1, **Figure 2**) the generated charge carriers form non-equilibrium distributions in their respective bands.[13] These distributions quickly equilibrate into Fermi–Dirac distributions, defined by respective temperatures T_e and T_h (Step 2, Figure 2). This process is defined as carrier thermalization, as one can now assign a temperature to the

T. Faber, L. J. A. Koster
Zernike Institute for Advanced Materials
University of Groningen
Nijenborgh 4, 9747 AG Groningen, The Netherlands
E-mail: l.j.a.koster@rug.nl

L. Filipovic
CDL for Multi-Scale Process Modeling of Semiconductor Devices and Sensors at the Institute for Microelectronics
TU Wien
Gusshausstrasse 27-29, 1040 Vienna, Austria

ADVANCED
SCIENCE NEWS
www.advancedsciencenews.com

Solar
RRL

www.solar-rrl.com

Table 1. Selection of observed experimental cooling times in metal halide perovskites, compared to GaAs.[6]

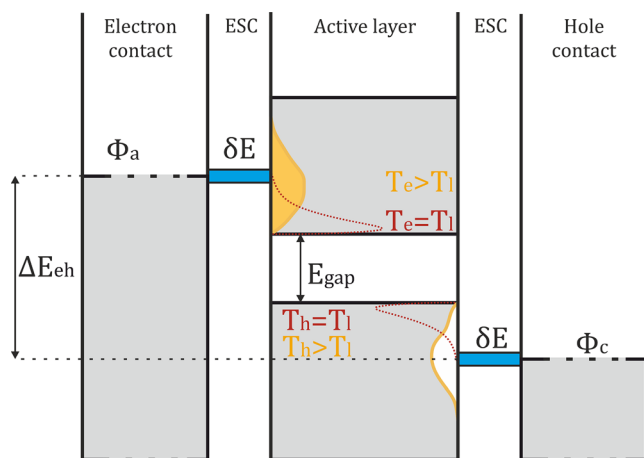|	Relaxation times to 600 K [ps]	Carrier density [ρ in 10^{17} cm^{-3}]	Dielectric constants [$\varepsilon_\infty/\varepsilon_0$]	Carrier (electron) effective mass [m^*]	Phonon frequency [$\omega_0/2\pi$ in THz]
GaAs	0.1	1	7.9[61]/12[61]	0.067[62]	8.15[63]
MAPbI$_3$ s	0.6	5.2	4.5[41]/25.7[40]	0.15[40]	2.25[10]
–	60	60	–	–	–
	1.1	64			
MAPbBr$_3$	0.8	150	6.7[64]/25[64]	0.27[47]	4.47[10]
–	200	0.7	–	–	–
CsPbI$_3$	2	7	6.1[10]/18.1[10]	0.17[65]	2.57[10]
–	10	70	–	–	–
FAPbI$_3$	40	11	6.6[66]/–	0.1[67]	2.25[68]
FASnI$_3$	1000	60	3.58[69]/–	0.17[69]	–

Figure 1. The design of a hot carrier solar cell consists of an active layer wedged between two energy selective contacts (ESC). These ESCs are aligned with the hot carrier distributions (yellow). These distributions are at elevated temperatures T_e and T_h, compared to the regular, cooled down, distributions (red) at lattice temperature T_l. The corresponding energy difference between the two quasi–Fermi levels is therefore larger resulting in a higher open circuit voltage.

distribution (Often the relaxation timescale is referred to as the thermalization time,[15] referring to the thermalization losses which occur when the carrier cools down. However this is physically not accurate. Thermalization is the process of acquiring a temperature, hence we therefore stick to the definition stated earlier, following Ref. [5]). Carrier thermalization can occur via carrier–carrier, carrier–phonon, and carrier–impurity scattering.[16] In the case of MHPs, carrier–carrier scattering is assumed to be the dominating process, due to their relatively low optical dielectric constant, resulting in weaker Coulomb screening.[16] Thermalization occurs on a fs to a sub-ps timescale and is expected to occur much faster than the relaxation process.[17] It is important to note that thermalization is a continuous process, which continues to influence the cooling dynamics even after the carriers are cooled down via carrier–phonon interactions (Step 3, Figure 2). In polar semiconductors, such as MHPs,

relaxation predominantly occurs via the Fröhlich interaction with longitudinal optical (LO) phonons.[18,19]

Understanding carrier thermalization is of central importance for the realization of HCSCs. The reason for this is twofold: 1) fast thermalization is an essential ingredient in HCSCs for successful operation under steady-state conditions.[20] Carriers can be extracted, provided that their energy lies within the window of energies accepted by the ESC. As a result, the carrier distribution is influenced by the rate of extraction at the energy level of the ESC. For optimal performance, the extraction level should be repopulated sufficiently quickly. This is done by rethermalization of the carriers.[20] It is essential to understand how one should tune the material, in order to achieve fast thermalization times, while keeping cooling times extended and 2) in ultrafast spectroscopy experiments, thermalization via carrier–carrier interactions also plays an important role in the cooling dynamics of HCSCs.[16,21] As was noted by Richter et al.,[16] and emphasized by Ulatowski et al.,[21] an increase in the degree of background doping could play a detrimental role on the cooling time. Carriers would lose their surplus energy much faster as they now thermalize not only among other non-equilibrium carriers, but also with a background of carriers, resulting in a much lower T_e/T_h. Essentially, additional cooling occurs via thermalization. Insight in this effect could particularly be important for the analysis on the suitability of tin based perovskites for HCSCs. Tin based perovskites have shown very long cooling times[12]; however, the oxidation of Sn^{2+} to Sn^{4+} inherently produces a large background ensemble of cold holes,[22,23] which could be detrimental for the hot carrier dynamics.[21,24]

In this manuscript, we investigate both processes mentioned earlier, in order to understand the role that thermalization plays in the hot carrier (HC) dynamics of a theoretical HCSC. For this, we make use of an ensemble Monte Carlo (EMC) simulation framework.[25–30] The EMC technique is a proven numerical method, when dealing with charge transport in semiconductors,[31] especially when it comes to far-from-equilibrium transport.[25] Mainly due to its adjustability, and the full description of x and k space, when treating scattering, the EMC method is an excellent tool to investigate scattering mechanisms and their respective interplay. Over the years, it has been frequently used
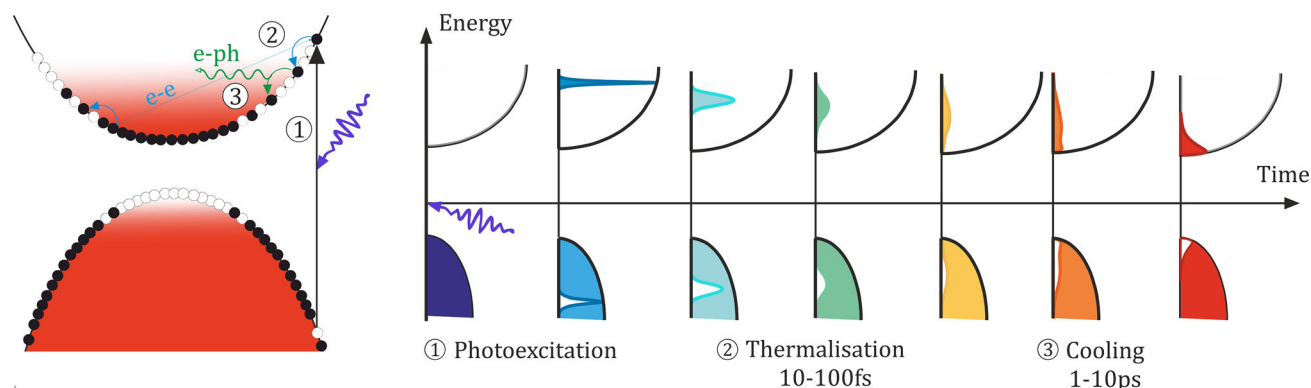
Figure 2. General picture of hot carrier dynamics in a semiconductor. Carriers are photo-excited at Step 1, forming non-equilibrium distributions in the respective bands. Carriers subsequently thermalize into Fermi–Dirac distributions characterized by a temperature at Step 2. For MHPs, thermalization is dominated by carrier-carrier interactions. Finally, at Step 3, carriers cool down towards the lattice temperature via carrier-phonon interactions, before they eventually recombine.

to deal with hot carrier problems,[25,32–34] for example in studies of hot carrier trends in metal oxide semiconductor field effect transistors,[34] or more closely related to our investigation, when modeling the electron–hole interactions on the ultrafast relaxation of hot photoexcited carriers in GaAs.[32] However in the field of MHPs, thus far EMC has only been used in order to quantify the effect of polaron formation on the mobility of charge carriers.[35]

The EMC fully takes into account both scattering and transport processes and is therefore the necessary next step in accurately describing the cooling process of hot carriers in MHPs.[19] Our model consists of carrier–carrier scattering and carrier×LO–phonon interactions, as thermalization is governed by the former and relaxation by the latter. In this manuscript, we focus on using MHPs as an absorber material in order to contribute to the recent developments on reported slow HC cooling of MHPs; however, we note that our discussion has broader implications since we discuss optimal properties required of a suitable absorber material for HCSCs.

We begin by visualizing the HC dynamics in a MAPbI$_3$-like system, where we observe similar relaxation times as those documented experimentally. Our study is finally able to bridge experimentally-observed hot carrier behavior with theoretical understanding. An interpretation of the results obtained with HC experiments relies heavily on HC theory. Therefore, a direct simulation and visualization on how exactly theoretical parameters impact the process is helpful for further interpretation and deeper understanding of observations and, ultimately, can inform on how to improve designs. We subsequently examine the thermalization process in detail. First, with a focus on reason 1 given earlier, we address the question of how one can achieve fast thermalization times while keeping relaxation times extended. We show the trends in the thermalization and relaxation times for several material parameters, mainly focusing on the effective mass and dielectric permittivity.

The effective mass is a measure of the band dispersion. As the conduction band minimum mainly consists of Pb 6p orbitals,[36] switching to another cation, such as Sn, causes the band edge to shrink and alters the band dispersion.[37] Furthermore, switching

the halide from I to Br to Cl also alters the band dispersion of the valence band,[37] as its maximum is mainly built up from hybridized I 5p orbitals.[38] Thus, by varying the effective mass over the documented range, we effectively modify the perovskite composition regarding different B-site cations and halides.

Additionally, swapping the B-site cation from Pb to Sn leads to a narrowing of the bandgap, and therefore an increase in optical dielectric constant.[39] Varying the optical dielectric constant is an additional means of gaining insight into the effect of swapping the B-site cation. Investigating the role of the B-site cation is important, as there is a large difference in cooling times documented in experimental reports for lead, and tin-based perovskites (see Table 1). Additionally, the optical dielectric constant is central in determining the carrier–phonon coupling strength.

These parameters were specifically chosen because they impact both carrier-carrier and Fröhlich interactions, causing the resulting effect on the thermalization and cooling process to be non-trivial. We find that a small effective mass, and thereby a sharp energy band, is desired for both fast thermalization and slow cooling. We show that the optical dielectric constant plays a more delicate role, as weaker screening results in faster thermalization, however could also increase relaxation rates as it could increase the carrier–phonon scattering rate. Second, we shift our investigation toward reason 2, as stated earlier. Here, we show and quantify the effect of thermalization with a cold-background ensemble on the cooling time, concluding that the effect is significant while being highly density dependent. Our work provides insights on the ongoing discussion on cooling times of MHPs, and the obtained theoretical understanding is meant to provide a stepping-stone toward finally designing a working HCSC.

2. Results and Discussion

Our investigation starts with the visualization of the hot carrier cooling dynamics for metal halide perovskites, particularly within a typical MAPbI$_3$ like system. Our motivation for the focus on a MAPbI$_3$-like system is that most studies of hot carrier cooling have been focused on this perovskite. We define a MAPbI$_3$-like system through its effective mass m^*, dielectric

constant ε_∞, and typical phonon frequency ω_0. The principle aim of the visualization is to understand whether or not the cooling process of MAPbI$_3$ can accurately be described using EMC simulations. Our initial material consists of an ensemble of carriers, both electrons and holes, in thermal equilibrium, interacting via carrier–phonon coupling and carrier–carrier interactions, at a temperature of 300 K. The carriers have an effective mass of $m^* = 0.15$ both for electrons and holes.[40] The optic and static parts of the dielectric constants are given by $\varepsilon_\infty = 4.5$,[40,41] $\varepsilon_0 = 25.7$, respectively, and the typical phonon frequency for MAPbI$_3$ is given by $\omega_0/2\pi = 2.25$ THz.[10] The simulations are initiated, at time $t = 0$, with an energy pulse of 0.2 eV, exciting the entire ensemble. Here, we give all the particles a kinetic energy of 0.2 eV and randomize their momenta in all three spatial directions. Subsequently, we track the position and momenta of all particles over a period of 1 ps. The temperature of the system can be obtained by fitting the kinetic energy distribution to a Maxwell–Boltzmann distribution, defined by a temperature. Moreover, the fitting procedure consequently also yields the degree of thermalization. By tracking how accurately the energy distribution fits to a Maxwell–Boltzmann distribution over time, we are able to measure the degree of the thermalization over time.

In **Figure 3** we display the resulting particle energy distribution for carrier densities of $\rho = 10^{16}$ cm^{-3}, and $\rho = 10^{18}$ cm^{-3}, where the former corresponds to a carrier–phonon dominated regime, and the latter to a carrier–carrier dominated one. With higher particle densities, carrier–carrier interactions are expected to become more and more dominant, as the Coulomb interaction scales with $\rho^{\frac{1}{3}}$. Figure 3a,c describe the evolution of the energy distribution, while Figure 3b,d show the

temperature of the system over time. In Figure 3b,d, the fitting error is plotted around the fitted temperature as a measure of the thermalization.

From Figure 3, one can observe the different stages of the cooling process as described earlier. At $\rho = 10^{16}$ cm^{-3} (Figure 3b) we observe the system to thermalize within about 200 fs, while cooling down from approximately 2000 to 300 K occurs within around 1 ps. At $\rho = 10^{18}$ cm^{-3} (Figure 3d) thermalization is much faster, at about ≈40 fs; however, the cooling time is on the same scale. We note that our result at $\rho = 10^{16}$ cm^{-3} is in good agreement with experimental values found for MAPbI$_3$, as Yang et al. report values of 0.6 ps for cooling down from 1500 to 600 K at a density of 10^{17} cm^{-3}.[8] However, cooling times reported by Yang et al. significantly increase for higher densities, while our cooling times do not show the same behavior. The authors attribute the extended cooling times to a hot-phonon bottleneck effect.[42,43] The hot-phonon bottleneck effect is a term used to encompass all phenomena, which lead to a increased probability of phonon re-absorption, due to a non equilibrium phonon population which comes into play above a critical density.[42,43] Yang et al. found that the critical density is at $\rho \approx 5 \cdot 10^{17}$ cm^{-3}.[8] The hot-phonon bottleneck effect is a second-order effect, where phonon–phonon interactions play a crucial role. Our model does not include phonon–phonon interactions, since the focus of this paper is the interplay between carrier–phonon and carrier–carrier interactions. As such, a discussion on this difference is beyond the scope of the presented model.

Unlike for cooling times, we do observe a density dependence in the thermalization time. A visual comparison between
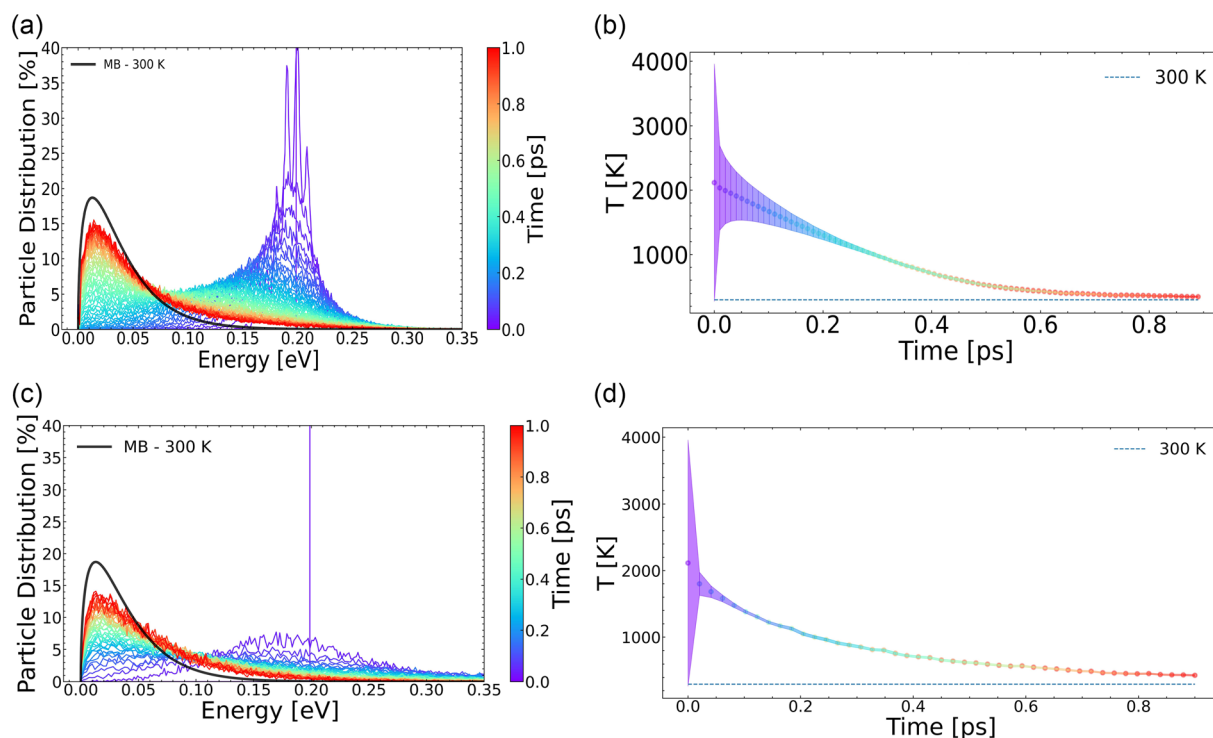

Figure 3. The cooling dynamics of MAPbI$_3$ ($m^* = 0.15$, $\varepsilon_\infty = 4.5$, $\varepsilon_0 = 25.7$, and $\omega_0 = 2.25$ THz) with a,c) the energy distribution for $\rho = 10^{16}$, and 10^{18} cm^{-3} and b,d) the temperature evolution over time for $\rho = 10^{16}$, and 10^{18} cm^{-3}.

Figure 3a,c makes it evident how much faster the higher density distribution takes on a smoothed form. The discrete nature of the energy spectrum shown in Figure 3a at early times indicates that timescales of carrier–phonon and carrier–carrier interactions for these systems at this density are comparable. The more continuous distribution at higher density (Figure 3c) points to carrier–carrier interactions being the dominant process behind thermalization. In this limit, the thermalization time depends on the number of scattering events between carriers per unit of time, which is obviously increased for higher carrier densities. This is also consistent with experimental results at this density for perovskites.[16] Unsurprisingly, this shows qualitatively and quantitatively that higher charge densities in the HCSC absorber material lead to faster cooling times.

Our result on the density dependence on the thermalization time invites us to return to the question of how a material should be tuned in order for it to have fast thermalization, while preserving slow cooling, being essential for the realization of HCSCs. Even though thermalization is dominated by carrier–carrier interactions, it is not completely determined by it. As one can see from Figure 3a,b, the thermalization times are about 2–3 times shorter than the cooling times, indicating also the relevance of carrier–phonon interactions on the thermalization process. In perovskite-like systems, thermalization is dominated by carrier–carrier interactions, while cooling is dominated by LO–phonon coupling.

In **Figure 4** and **5**, we show the impact of the effective mass and the dielectric constant on the thermalization time, respectively, for different densities. At time $t = 0$, the entire ensemble was excited to an energy of 0.2 eV, and the temperature of the system was subsequently calculated and extracted every 10 fs
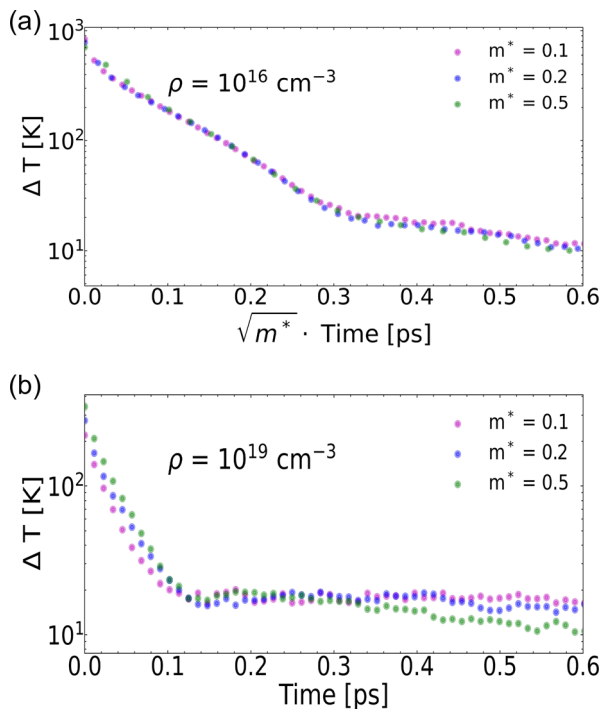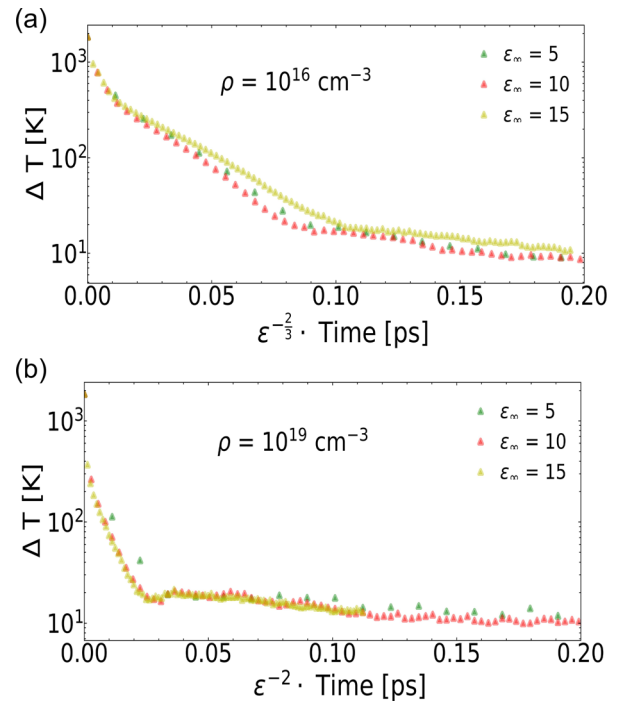

Figure 5. Thermalization times for different values of the dielectric constant ε_∞ for different densities a) $\rho = 10^{16}$ and b) $\rho = 10^{19}$ cm^{-3}.

for a period of 1 ps. In Figure 4 and 5, ΔT represents the deviation of the current energy distribution from that of a Maxwell–Boltzmann distribution. ΔT is the value of the fitting error (as determined by the fitting routine) of the fitted temperature of the energy distribution. As defined earlier, when $\Delta T \rightarrow 0$, the state becomes thermalized. Plotting this over time, yields a measure of the thermalization time. Simulations were performed for different values of the effective mass ($m^* = 0.1$, 0.2, 0.5) and the dielectric constant ($\varepsilon_\infty = 5, 10, 15$) at different particle densities ($\rho = 10^{16}$ cm^{-3}, 10^{19} cm^{-3}).

We perform simulations at even higher densities, in order to observe what happens in the limit where carrier–carrier interactions are strongly dominant. At these carrier densities (i.e., 10^{19} cm^{-3}), one enters from the classical Maxwell–Boltzmann regime into the quantum mechanical Fermi–Dirac regime when describing the particle statistics. Fermi–Dirac and Bose-Einstein statistics should be considered when solving the Boltzmann transport equation in this case.[44] However, in this study, we are primarily interested in high-energy (and hence high temperature) particle interactions. At sufficiently high temperatures, there are considerably more energy states than particles. Therefore, the vast majority of states are empty, resulting in a much higher likelihood of an energy state being empty than it containing two particles attempting to occupy the same level. Effectively, the Fermi–Dirac and Bose–Einstein statistics give the same result. This limiting result approaches Maxwell–Boltzmann statistics, which assumes that particles can be treated classically, since, at sufficiently high temperatures, the exponential term in the denominator of Fermi–Dirac statistics approaches $\exp(-E/kT)$, which is represented in the

Figure 4. Thermalization times for different values of the effective mass m^* for different densities a) $\rho = 10^{16}$ cm^{-3} and b) $\rho = 10^{19}$ cm^{-3}.

Maxwell–Boltzmann distribution.[45] The values of the material parameters span over a range corresponding to perovskite-like systems, i.e., polar semiconductors are characterized by relatively low effective masses ($m^* < 0.5$) and a low degree of screening ($\varepsilon_\infty \leq 15$).

The impact of the effective mass is provided in Figure 4a,b for low and high charge densities, respectively. At a density of $\rho = 10^{16}$ cm^{-3} (Figure 4a), we observe that thermalization takes place faster for a larger effective mass. Due to the low particle density, carrier–phonon interactions might be the dominant interaction mechanism. The LO–phonon scattering rate provided in Equation (1) suggests a $\sqrt{m^*}$ dependency for LO–phonon dominated processes. As we plot the low-carrier density data against time$\cdot\sqrt{m^*}$), we obtain an excellent agreement (Figure 4a), confirming our assumption that the thermalization dynamics at lower charge densities are driven by carrier–phonon coupling. The observation of carrier–phonon interactions dominating the process can be supported by noting the relatively long timescales of the thermalization time in this limit. Therefore, at this carrier density ($\rho = 10^{16}$ cm^{-3}), a small effective mass is desired when designing HCSCs.

At a high carrier density $\rho = 10^{19}$ cm^{-3} (Figure 4b), the thermalization time is found to be independent of the effective mass. More accurately, the phonon $\sqrt{m^*}$ dependency is compensated by a $1/\sqrt{m^*}$ dependency coming from the carrier-carrier scattering rate.[46] We observe thermalization times to be faster in this limit, supporting the hypothesis of a regime change. Further support can be obtained by looking at Figure S1, Supporting Information, where the dependency of the effective mass on the thermalization time for a system with only carrier–carrier interactions is clearly shown to follow a $1/\sqrt{m^*}$ trend. This is in agreement with the established theory on the carrier–carrier scattering rate.[46] For HCSCs operating at the high charge density regime, a large effective mass is thus less critical for the thermalization time. However, a large effective mass still causes accelerated cooling; therefore, a small effective mass is also desired at a high carrier density ($\rho = 10^{19}$ cm^{-3}), when designing a suitable absorber material for HCSCs.

We further analyze our results for the dielectric constant in Figure 5. Generally, it can be observed that the thermalization time scales inversely with the dielectric constant. As particles experience less screening, they thermalize faster. We find a $\varepsilon_\infty^{-3/2}$ dependence for the data at a low density (Figure 5a) and a ε_∞^{-2} dependence at a high density (Figure 5b). Both dependencies fit the data very well; however, an insightful nuance regarding interaction regimes can be distilled from the two different dependencies. The $\varepsilon_\infty^{-3/2}$ fit corresponds to a regime where the carrier-phonon interactions are balanced by the carrier–carrier interactions. The dependencies on ε_∞ for the LO–phonon coupling and Coulomb interaction are ε_∞^{-1}, noted in Equation (1), and ε_∞^{-2},[46] respectively. A $\varepsilon_\infty^{-3/2}$ dependency (Figure 5a) would indicate a regime where both interactions are exactly balanced. By looking more closely at the high-density data (Figure 5b), one can observe that the overlap between the $\varepsilon_\infty = 10$ (yellow line) and the $\varepsilon_\infty = 15$ (red line) is actually more precise. This perfect fit for a ε_∞^{-2} dependency suggests a carrier–carrier dominated regime, following similar reasoning as above.

Intuitively, it could be argued that for a higher degree of screening, a drift away from a carrier–carrier dominated regime would be expected, as the Coulomb interaction scales inversely proportional with the dielectric of the material. However, also the carrier–phonon interactions are diminished by a larger ε_∞, i.e., eps$_{inf}$ is in the denominator of Equation (1). Moreover, as the Fröhlich interaction is proportional to the difference between the static and the optic part of the dielectric constant, noted in Equation (1), the $1/\varepsilon_\infty$ proportionality is only valid in the limit where $\varepsilon_\infty \ll \varepsilon_0$. When $\varepsilon_0 = 25$, in these simulations, the values of ε_∞ approach the asymptotic limit. In fact, an increase in ε_∞ from 5 to 15 results into a decrease in $P_{e,LO}$ by a factor of 9. One can conclude that the increased Coulomb screening is eclipsed by a decrease in carrier–phonon interaction, resulting in a carrier–carrier dominated regime for higher values of the dielectric constant. From these results, one can conclude that when designing HCSCs, a material with both low static and optic parts of the dielectric constant is desired. In this way, one obtains fast thermalization, while keeping cooling times extended.

The LO–phonon interaction strength plays an important role in distinguishing between different regimes. Therefore, also a quantity such as the phonon frequency ω_0 impacts these results, as a large phonon frequency results in a stronger phonon coupling.

The results presented here show how significant carrier–phonon interactions can be for thermalization in low particle density perovskite systems and in determining the feasibility and performance of HCSCs. In the high particle density regime, which is generally the operating regime for a HCSC, the influence of carrier–phonon interactions is less significant. In this regime, a small effective mass is desired since it slows down cooling, does not negatively impact thermalization, and enhances the carrier mobility. These results suggest that perovskites which contain a lighter halide are more suitable for designing HCSCs, since a heavier halide increases the effective mass. Also, swapping from lead to tin could be fruitful since this will in particular lower the hole effective mass.[47]

A low optic dielectric constant ε_∞ is desired for fast thermalization. However, in combination with a high static dielectric constant ε_0, it could result in fast cooling. It would be informative to see how these results would alter in a system where phonon–phonon interactions are incorporated, as in this case perhaps strong LO–phonon coupling is desired for a fast population of non-equilibrium phonon modes.[8]

Finally, the effect a cold background ensemble of carriers can have on the cooling dynamics of newly excited carriers is discussed. We have performed simulations on a thermal ensemble of carriers at 300 K of a perovskite-like system. As previously, we start by introducing an energy pulse of 0.2 eV and observing the cold background effect by varying the background density ρ_{cold}. The density of the ensemble which is excited by the energy pulse is labeled as ρ_{photo}. We track the normalized temperature T/T_0 over time, in order to observe whether or not there is a different cooling gradient in the initial thermalization phase. We show the cold background (CB) effect in **Figure 6** for two different density regimes. We only plot the first 0.25 ps because the effect ceases as soon as thermalization is completed.

Our results indicate a strong cold background effect at a high background density. Figure 6a shows our results for a low carrier
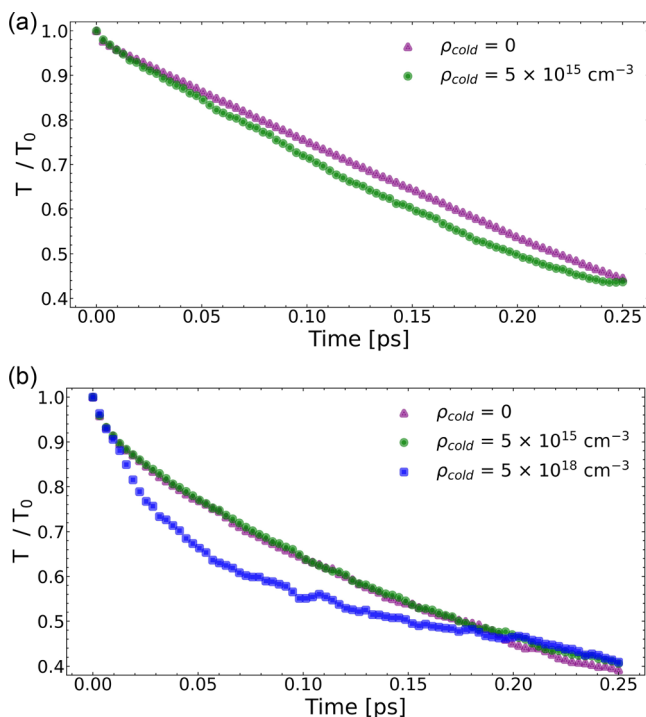
Figure 6. Normalized temperature over time after initiating an energy pulse for a perovskite-like system with different background densities ρ_{cold}. Simulations are performed for different excitation densities a) $\rho_{photo} = 10^{16}$ cm^{-3} and b) $\rho_{photo} = 10^{19}$ cm^{-3}.

density $\rho_{photo} = 10^{16}$ cm^{-3}. We do not observe any significant difference in the cooling slope, when we vary the background density from 0 to 5×10^{15} cm^{-3}. A further increase in the background density to 5×10^{18} cm^{-3} would give meaningless results, as the energy pulse in a system like this would be comparable to a perturbation. At a high carrier density $\rho_{photo} = 10^{19}$ cm^{-3} (Figure 6b), we note a strong effect at short times. When the background density is increased from 5×10^{15} to 5×10^{18} cm^{-3}, we observe a steeper cooling slope for the first 0.1 to 0.2 ps. We can attribute the different results at different densities to the fact that the CB effect is governed by carrier–carrier interactions, which are highly density dependent in nature, as we have already observed in the thermalization times of MAPbI$_3$ (Figure 4b,d). Likewise, other parameters, such as the dielectric constant and the effective mass, which impact the carrier–carrier scattering rate, enhance this effect. However, as they also impact the phonon cooling rate, it is more difficult to directly quantify their impact on the CB effect.

Our findings confirm several important experimental results in understanding the large differences found for relaxation times in tin-perovskites. The self-doping property of tin via the oxidation of Sn^{2+} to Sn^{4+} could result into the formation of a large cold background ensemble of holes.[22,23] The degree of background doping has been put forward to address the wide range of observed cooling times.[21,24] Our results show accelerated cooling during the first scattering phase for high background density systems, which confirms the hypothesis used by

Kahmann et al.[24] and Ulatowksi et al.[21] to explain the shorter cooling times for tin-based perovskites.

The strong density dependence for this effect makes it possible to limit its consequences by choosing an operating regime where carrier–carrier interactions do not dominate the thermalization process. However, as fast thermalization is also a key ingredient for the successful operation of a HCSC, this could become quite difficult. We note that a cold background ensemble only forms if the operation of the HCSC is not optimal. In theory, carriers should be extracted before they reach the bottom of the energy band, and fast thermalization is an essential component to repopulate the extraction energy level. Our results emphasize the critical role of sample purity in the cooling process in HCSCs. This effect could help explain the large range of cooling times that have been found experimentally (see Table 1).

As a final note, it is important to mention the topic of polarons. Polaron formation has also been identified as a separate process in the cooling dynamics in MHPs and has been put forward as a potential mechanism behind the slow cooling times.[9,48–52] The incorporation of polarons into the EMC model would be a relevant, though complicated, addition. Polaron formation could impact both thermalization and cooling, as the effective mass of carriers is altered.[53] A detailed description of the cooling dynamics for a polaronic carrier landscape would be a fruitful next step, but lies beyond the scope of this manuscript.

3. Conclusions

In this contribution we used ensemble Monte Carlo simulations to investigate the role of thermalization on carrier cooling dynamics for perovskite-like systems. First, we have visualized the thermalization and cooling process of MAPbI$_3$ at different charge carrier densities. Second, we have shown how thermalization times depend on different material parameters, and we have extracted trends showing how to optimize the thermalization time. Our work puts emphasis on the fact that thermalization and cooling are not two separated stages, but interconnected processes. By studying their interplay, we have qualified and quantified the impact of carrier–phonon interactions on the thermalization process.

We can conclude that for the design of HCSCs, a small carrier effective mass is desired. Our analysis on the dielectric constant showed that a low dielectric constant ε_∞ would enhance thermalization; however, it could also accelerate carrier cooling. Finally, we have quantified how thermalization can act as a cooling mechanism via the cold-background effect. Here, we assessed that the effect is highly density dependent and only starts playing a role at high carrier densities and a high background density of $\rho = 10^{19}$ cm^{-3}. These findings help to explain the large differences reported in relaxation times for tin perovskites. Our work effectively maps out how perovskites should be tuned, regarding their material parameters, carrier concentration, and purity, in order for them to be used in the optimal way to realize a HCSC.

4. Experimental Section

For simulations, ensemble Monte Carlo code ViennaEMC was used.[54] The ensemble Monte Carlo method[26] solves the Boltzmann transport

equation without a priori assumptions regarding the form of the distribution function and offers the implementation of complex band structures,[27] making it a highly accurate method for studying the time-evolution of a statistical ensemble.[55] The EMC method models the motion of an ensemble of electrons as a sequence of randomly generated free flights, interrupted by randomly selected scattering events.[55] For the generation of random numbers, a long period (2×10^{18}) L'Ecuyer random number generator[56] was used with Bays–Durham shuffle and added safeguards. In the EMC, an entire ensemble of particles is simulated one after the other for the period of one timestep, tracking both x and k space coordinates. The method is semi-classical as the free flight is modeled classically, while the scattering rates are computed quantum mechanically via Fermi's Golden Rule.[26] The scattering rates are energy dependent, pre-computed, and stored at intervals of 0.4 meV in look-up tables. The model consists of scattering via LO–phonon interactions, described by Fröhlich interactions, and carrier–carrier interactions via Coulomb interactions. The LO–phonon scattering rate for both absorption and emission is given by[26]

$$P_{e,LO}(E) = \frac{e^2\sqrt{m^*}\omega_0}{\sqrt{2}\hbar}\left(\frac{1}{\varepsilon_\infty}-\frac{1}{\varepsilon_0}\right)\mathbf{F}(E,E')[N_{op}+\frac{1}{2}\mp\frac{1}{2}] \quad (1)$$

where e is the elementary charge, m^* is the effective mass, ω_0 is the typical phonon frequency, and ε_∞ and ε_0 are the optical and static parts of the dielectric constant, respectively. The phonon number is given by N_{op} for absorption (−) and $N_{op}+1$ for emission (+). Finally, E is the energy and $\mathbf{F}(E,E')$ is a function of the energy E before, and after the E' interaction with a phonon, where $E' = E \pm \hbar\omega_{op}$ for absorption (−) and emission (+), respectively.

The carrier–carrier interactions were modelled classically using the Fast-Multipole Method (FMM) using the ScalFMM library.[57] The FMM handles particles via direct compution at close range, while clusters of distant particles are grouped together and approximated by the use of a multipole expansion.[58] More information on how the FMM is implemented in detail can be found in the original paper of Rohklin.[58] Since the FMM models the carrier–carrier interactions classically, the electric field is recomputed after every timestep, before each free-flight phase commences. A $(r+a)$ kernel was used, with a cut-off radius of $a = 1$ nm. When using the FMM, the carriers may experience artificial heating, since they can get too close to each other during a timestep.[59,60] With a cut-off radius of $a = 1$ nm the issue is resolved, without impacting physical accuracy, as one still remains well under the average interparticle distance. The Coulomb potential can then be represented as

$$V_c(r) = \frac{q}{4\pi\varepsilon(r+a)} \quad (2)$$

The dielectric constant ε used in the carrier–carrier interactions was taken to be equal to the optical part of the dielectric constant ε_∞, which also returns in the LO–phonon scattering rate. In the simulations, the multipole expansion was solved up to the second order, resulting in a maximum computation error of 10^{-2} for the potential, without the introduction of an external field. Ensembles of 10 000–100 000 particles, consisting of 50% holes and 50% electrons, were simulated in a 100 nm to 1 μm box, which was periodically repeated in all three directions 384 times. A parabolic band structure approximation was used, defined by an effective mass. The particle dynamics are then described by

$$v = \frac{1}{\hbar}\nabla_k E(k) = \frac{\hbar k}{m^*} \quad (3)$$

and

$$r(t) = r(0) + vt + \frac{qE(r)}{2m^*}t^2 \quad (4)$$

where r is the position, k is the momentum, $\hbar$ is the reduced Planck constant, $\mathbf{E}(k)$ is the electric field, m^* is the effective mass in terms of the

electron mass m_e, and t is the time. These equations were solved for each timestep (0.1 fs) for the entire simulation time. The obtained particle energy distribution was fitted to a MB distribution to obtasin a temperature (The fitting to a Maxwell–Boltzmann distribution was performed in Python using the SciPy function curve_fit).

Supporting Information

Supporting Information is available from the Wiley Online Library or from the author.

Conflict of Interest

There are no conflicts to declare.

Data Availability Statement

The data that support the findings of this study are available from the corresponding author upon reasonable request.

[1] S. Kahmann, M. Loi, *J. Mater. Chem. C* **2019**, *7*, 2471.
[2] W. Shockley, H. J. Queisser, *J. Appl. Phys.* **1961**, *32*, 510.
[3] P. Würfel, *Physik der Solarzellen*, Spektrum Akademischer Verlag, Germany **2000**.
[4] R. T. Ross, A. J. Nozik, *J. Appl. Phys.* **1982**, *53*, 3813.
[5] J. Nelson, *The Physics of Solar Cells*, World Scientific Publishing Company, Singapore **2003**.
[6] M. Li, J. Fu, Q. Xu, T. C. Sum, *Adv. Mater.* **2019**, *31*, 1802486.
[7] K. Wang, D. Yang, C. Wu, M. Sanghadasa, S. Priya, *Prog. Mater. Sci.* **2019**, *106*, 100580.
[8] Y. Yang, D. Ostrowski, R. France, K. Zhu, J. van de Lagemaat, J. Luther, M. Beard, *Nat. Photonics* **2015**, *10*, 53.
[9] D. Niesner, H. Zhu, K. Miyata, P. P. Joshi, T. J. S. Evans, B. J. Kudisch, M. T. Trinh, M. Marks, X.-Y. Zhu, *J. Am. Chem. Soc.* **2016**, *138*, 15717.
[10] J. Frost, *Phys. Rev. B* **2017**, *96*, 195202.
[11] J. Fu, Q. Xu, G. Han, *Nat. Commun.* **2017**, *8*, 1300.

[12] H. Fang, S. Adjokatse, S. Shao, J. Even, M. Loi, *Nat. Commun.* **2018**, *9*, 243.

[13] D. König, K. Casalenuovo, Y. Takeda, G. Conibeer, J. Guillemoles, R. Patterson, L. Huang, M. Green, *Physica E* **2010**, *42*, 2862.

[14] S. C. Limpert, S. P. Bremner, *Appl. Phys. Lett.* **2015**, *107*, 073902.

[15] G. Conibeer, S. Shrestha, S. Huang, R. Patterson, H. Xia, Y. Feng, P. Zhang, N. Gupta, M. Tayebjee, S. Smyth, Y. Liao, S. Lin, P. Wang, X. Dai, S. Chung, *Sol. Energy Mater. Sol. Cells* **2015**, *135*, 124.

[16] J. M. Richter, F. Branchi, F. Valduga de Almeida Camargo, B. Zhao, R. H. Friend, G. Cerullo, F. Deschler, *Nat. Commun.* **2017**, *8*, 376.

[17] L. Rota, P. Lugli, T. Elsaesser, J. Shah, *Phys. Rev. B* **1993**, *47*, 4226.

[18] H. Fröhlich, N. F. Mott, *Proc. R. Soc. London Ser. A. Math. Phys. Sci.* **1939**, *172*, 94.

[19] T. Wang, L. Jin, J. Hidalgo, W. Chu, J. M. Snaider, S. Deng, T. Zhu, B. Lai, O. Prezhdo, J.-P. Correa-Baena, L. Huang, *Sci. Adv.* **2020**, *6*, abb1336.

[20] Y. Takeda, T. Motohiro, D. König, P. Aliberti, Y. Feng, S. Shrestha, G. Conibeer, *Appl. Phys. Express* **2010**, *3*, 104301.

[21] A. M. Ulatowski, M. D. Farrar, H. J. Snaith, M. B. Johnston, L. M. Herz, *ACS Photonics* **2021**, *8*, 2509.

[22] Y. Takahashi, H. Hasegawa, Y. Takahashi, T. Inabe, *J. Solid State Chem.* **2013**, *205*, 39.

[23] T. Leijtens, R. Prasanna, A. Gold-Parker, M. F. Toney, M. D. McGehee, *ACS Energy Lett.* **2017**, *2*, 2159.

[24] S. Kahmann, S. Shao, M. A. Loi, *Adv. Funct. Mater.* **2019**, *29*, 1902963.

[25] D. K. Ferry, *Hot Carriers in Semiconductors*, IOP Publishing, USA **2021**, pp. 2053–2563, 7–1 to 7–49.

[26] C. Jacoboni, P. Lugli, *The Monte Carlo Method for Semiconductor Device Simulation, Computational Microelectronics*, Springer Vienna, USA **2011**.

[27] C. Jacoboni, L. Reggiani, *Rev. Mod. Phys.* **1983**, *55*, 645.

[28] K. Hess, *Monte Carlo Device Simulation: Full Band and Beyond*, Kluwer Academic Publishers, USA **1991**.

[29] R. Hockney, J. Eastwood, *Computer Simulation Using Particles*, CRC Press, USA **1988**.

[30] K. Tomizawa, *Numerical Simulation of Submicron Semiconductor Devices*, Artech House Publishers, USA **1993**.

[31] H. Kosina, M. Nedjalkov, S. Selberherr, *IEEE Trans. Electron Devices* **2000**, *47*, 1898.

[32] M. A. Osman, D. K. Ferry, *Phys. Rev. B* **1987**, *36*, 6018.

[33] P. Lugli, D. Ferry, *Phys. Rev. Lett.* **1986**, *56*, 1295.

[34] A. Duncan, U. Ravaioli, J. Jakumeit, *IEEE Trans. Electron Devices* **1998**, *45*, 867.

[35] L. A. D. Irvine, A. B. Walker, M. J. Wolf, *Phys. Rev. B* **2021**, *103*, L220305.

[36] C. Motta, F. El Mellouhi, S. Kais, N. Tabet, F. Alharbi, S. Sanvito, *Nat. Commun.* **2015**, *6*, 7026.

[37] S. Tao, X. Cao, P. A. Bobbert, *Sci. Rep.* **2017**, *7*, 14386.

[38] K. T. Butler, J. M. Frost, A. Walsh, *Mater. Horiz.* **2015**, *2*, 228.

[39] J. N. Wilson, J. M. Frost, S. K. Wallace, A. Walsh, *APL Mater.* **2019**, *7*, 010901.

[40] F. Brivio, K. T. Butler, A. Walsh, M. van Schilfgaarde, *Phys. Rev. B* **2014**, *89*, 155204.

[41] F. Brivio, A. B. Walker, A. Walsh, *APL Mater.* **2013**, *1*, 042111.

[42] W. Pötz, *Phys. Rev. B* **1987**, *36*, 5016.

[43] S. S. Prabhu, A. S. Vengurlekar, *Phys. Rev. B* **1996**, *53*, 7815.

[44] M. Zebarjadi, C. Bulutay, K. Esfarjani, A. Shakouri, *Appl. Phys. Lett.* **2007**, *90*, 092111.

[45] W. Vincenti, C. Kruger, *Introduction to Physical Gas Dynamics*, Wiley, USA **1965**.

[46] N. Del Fatti, C. Voisin, M. Achermann, S. Tzortzakis, D. Christofilos, F. Vallée, *Phys. Rev. B* **2000**, *61*, 16956.

[47] E. Mosconi, P. Umari, F. De Angelis, *J. Mater. Chem. A* **2015**, *3*, 9208.

[48] H. Zhu, K. Miyata, Y. Fu, J. Wang, P. P. Joshi, D. Niesner, K. W. Williams, S. Jin, X.-Y. Zhu, *Science* **2016**, *353*, 1409.

[49] J. M. Frost, L. D. Whalley, A. Walsh, *ACS Energy Lett.* **2017**, *2*, 2647.

[50] T. J. S. Evans, K. Miyata, P. P. Joshi, S. Maehrlein, F. Liu, X.-Y. Zhu, *J. Phys. Chem. C* **2018**, *122*, 13724.

[51] P. P. Joshi, S. F. Maehrlein, X. Zhu, *Adv. Mater.* **2019**, *31*, 1803054.

[52] A. Burgos-Caminal, J. M. Moreno-Naranjo, A. R. Willauer, A. A. Paraecattil, A. Ajdarzadeh, J.-E. Moser, *J. Phys. Chem. C* **2021**, *125*, 98.

[53] D. Emin, *Polarons*, Cambridge University Press, USA **2012**.

[54] L. Gollner, R. Steiner, L. Filipovic, https://github.com/ViennaTools/ViennaEMC (accessed: January 2023).

[55] K. Nederveen, *Ph.D. Thesis, Electrical Engineering*, Eindhoven University of Technology, **1989**.

[56] P. L'Ecuyer, *Commun. ACM* **1990**, *33*, 85.

[57] P. Blanchard, B. Bramas, O. Coulaud, E. F. Darve, L. Dupuy, A. Etcheverry, G. Sylvand, https://gitlab.inria.fr/solverstack/ScalFMM (accessed: June 2020).

[58] V. Rokhlin, *J. Comput. Phys.* **1985**, *60*, 187.

[59] C. Heitzinger, C. Ringhofer, S. Ahmed, D. Vasileska, *J. Comput. Electron.* **2004**, *11*, 24.

[60] L. Gollner, *MSc Thesis*, TU Wien, Vienna, Austria, **2023**.

[61] M. Levinshtein, S. Rumyantsev, M. Shur, W. Scientific, *Handbook Series on Semiconductor Parameters: Ternary and Quaternary III-V Compounds*, World Scientific Publishing Company, Singapore **1999**.

[62] A. Raymond, J. Robert, C. Bernard, *J. Phys. C Solid State Phys.* **2001**, *12*, 2289.

[63] T. Handa, T. Yamada, M. Nagai, Y. Kanemitsu, *Phys. Chem. Chem. Phys.* **2020**, *22*, 26069.

[64] D. Zhao, J. Skelton, H. Hu, *Appl. Phys. Lett.* **2017**, *111*, 201903.

[65] S. Ponce, M. Schlipf, F. Giustino, *ACS Energy Lett.* **2019**, *4*, 456.

[66] F. Ma, J. Li, W. Li, N. Lin, L. Wang, J. Qiao, *Chem. Sci.* **2017**, *8*, 800.

[67] K. Galkowski, A. Mitioglu, A. Miyata, P. Plochocka, O. Portugall, G. E. Eperon, J. T.-W. Wang, T. Stergiopoulos, S. D. Stranks, H. J. Snaith, R. J. Nicholas, *Energy Environ. Sci.* **2016**, *9*, 962.

[68] A. D. Wright, C. Verdi, R. L. Milot, G. E. Eperon, M. A. Perez-Osorio, H. J. Snaith, F. Giustino, M. B. Johnston, L. M. Herz, *Nat. Commun.* **2016**, *7*, 11755.

[69] A. Filippetti, S. Kahmann, C. Caddeo, A. Mattoni, M. Saba, A. Bosin, M. Loi, *J. Mater. Chem. A* **2021**, *9*, 11812.